


In the format provided by the authors and unedited.

Single-crystal Winterbottom constructions of nanoparticle superlattices

Diana J. Lewis ^{1,2}, Leonardo Z. Zornberg¹, David J. D. Carter² and Robert J. Macfarlane ¹ 

¹Department of Materials Science and Engineering, Massachusetts Institute of Technology (MIT), Cambridge, MA, USA. ²The Charles Stark Draper Laboratory, Cambridge, MA, USA. e-mail: rmacfarl@mit.edu

Supplementary Information

Single Crystal Winterbottom Constructions of Nanoparticle Superlattices

Diana J. Lewis[‡], Leonardo Z. Zornberg[†], David J.D. Carter[‡], and Robert J. Macfarlane^{*†}

*Address correspondence to rmacfarl@mit.edu

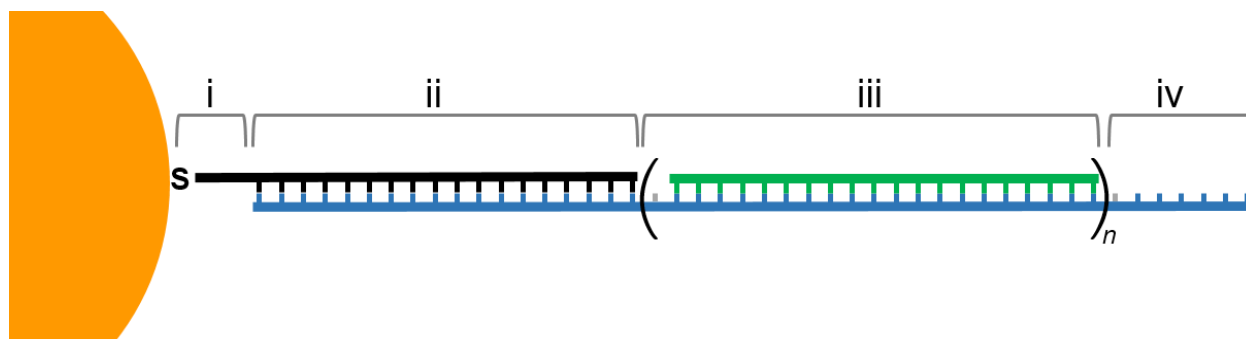
Contents

Supplementary Materials.....	2
1. DNA and Nanoparticle Information.....	2
2. Nanoparticle Functionalization Procedure.....	4
3. Linker Strand Preparation.....	5
4. AFM Imaging.....	5
5. Silica Embedding Procedure.....	5
Supplementary Note 1 - Equations and Analysis.....	6
1. Crystal Growth from Surfaces.....	6
2. Density of Nuclei on Surface.....	8
3. Winterbottom Construction Calculations.....	10
4. Analysis of Winterbottom Shape Change with Linker Density.....	11
5. Deviations from Winterbottom Construction Predicted Shape.....	12
6. Crystals Depositing from Solution.....	16
Supplementary Note 2- Additional Experiments.....	17
1. Crystal Size.....	17
2. Salt Concentration.....	18
3. Linker Density Exploration with FCC and <100> BCC.....	21
4. AlB ₂ experiments.....	23
5. Nucleation of Single Crystals at Surface Defect Sites.....	24
6. Surface-Induced Reorganization of Solution-Grown Wulff Polyhedra.....	25

Supplementary Materials

1. DNA and Nanoparticle Information

All DNA strands were procured from Integrated DNA Technologies (IDT). The method used to functionalize nanoparticles with DNA utilizes a two-strand design with a “sticky end” at the apex of the second strand to bind particles together.¹ This construction allows for nanoparticles to be functionalized with identical “anchor” strands, ensuring consistent loading at approximately 0.25 strands per square nanometer^{2,3}, or about 300 strands per 20-nm diameter nanoparticle. PAEs are then configured for specific lattice designs using the second linker strand (Supplementary Figure 1).



Supplementary Figure 1: DNA-NP (PAE) Motif. A short ‘anchor’ strand (black) is attached to the gold nanoparticle via a gold-sulfur bond and a spacer (i). A second ‘linker’ strand (blue) is attached to the first, containing three regions; a section complementary to the first (ii), a duplexed (green) variable length region (iii), and a sticky end (iv) that hybridizes with other particles.

The configuration of our system can be seen in Supplementary Figure 1 and consists of DNA strands with four distinct sections. The first strand, the ‘anchor strand’ (black) is an 18-base single-stranded DNA (ssDNA) that attaches to the gold nanoparticle through a gold-sulfur covalent bond and provides flexibility and density control through the length and design of section (i). For this work, section (i) consists of two Spacer 18s (18-atom hexaethyleneglycol chains linked via phosphate groups). The second strand (blue) is a ‘linker’ that has three regions; a complementary region that binds to the anchor strand (ii), a variable length intermediate section (iii) that serves as a spacer to vary the distance between nanoparticles, and a ~6-base ‘sticky end’ (iv) that binds to other DNA strands similarly attached to other nanoparticles. Alteration of the sticky end sequence can produce nanoparticles that are self-complementary or complementary to a second set of DNA-NPs. For the system used in this work, the length of section (iii) is increased by inserting 21-base sequence units until the desired length is reached (21 bases \cong 5 nm interparticle spacing). This intermediate section is duplexed with 20-base ‘duplexer’ strands (green), with one base left as a

single-strand section to act as a hinge between each rigid 20-base section (and the 18-base section (ii)). DNA sequences used in this work are listed in Supplementary Table 1.

Supplementary Table 1: DNA Sequences, color-coded to match anchor strands. Anchor Z was used for substrates, the other two for particles. Bold sequences at end of linkers indicate the sticky ends.

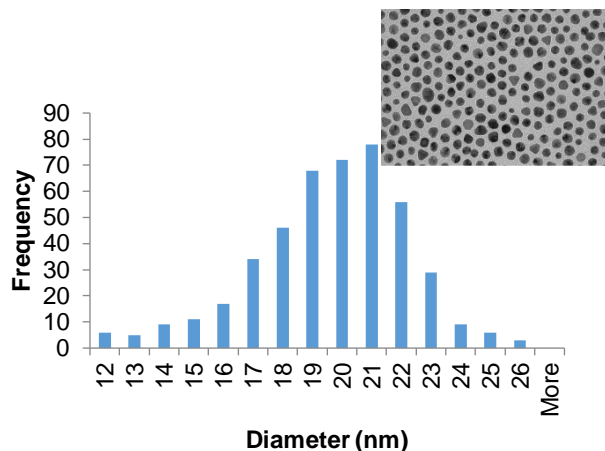
	DNA Type	Sequence (5'-3')
Anchor	Anchor HS-X	TCA ACT ATT CCT ACC TAC (EG6) ₂ -SH
	Anchor HS-Y	TCC ACT CAT ACT CAG CAA (EG6) ₂ -SH
	Anchor HS-Z	CGT ACA GTC GTT CGT ACT (EG6) ₂ -SH
Linkers for BCC, CsCl, AlB ₂	X-n1-A	GTA GGT AGG AAT AGT TGA A TTT AGT CAC GAC GAG TCA TT A TTCCTT
	X-n2-A	GTA GGT AGG AAT AGT TGA A TTT AGT CAC GAC GAG TCA TT A TTT AGT CAC GAC GAG TCA TT A TTCCTT
	X-n3-A	GTA GGT AGG AAT AGT TGA A TTT AGT CAC GAC GAG TCA TT A TTT AGT CAC GAC GAG TCA TT A TTT AGT CAC GAC GAG TCA TT A TTCCTT
	Y-n1-A'	TTG CTG AGT ATG AGT GGA A TTT AGT CAC GAC GAG TCA TT A AAGGAA
	Y-n2-A'	TTG CTG AGT ATG AGT GGA A TTT AGT CAC GAC GAG TCA TT A TTT AGT CAC GAC GAG TCA TT A AAGGAA
	Y-n3-A'	TTG CTG AGT ATG AGT GGA A TTT AGT CAC GAC GAG TCA TT A TTT AGT CAC GAC GAG TCA TT A TTT AGT CAC GAC GAG TCA TT A AAGGAA
	Z-n2-A	AGT ACG AAC GAC TGT ACG A TTT AGT CAC GAC GAG TCA TT A TTT AGT CAC GAC GAG TCA TT A TTCCTT
	Z-n2-A'	AGT ACG AAC GAC TGT ACG A TTT AGT CAC GAC GAG TCA TT A TTT AGT CAC GAC GAG TCA TT A AAGGAA
FCC Link	X-n2-B''	GTA GGT AGG AAT AGT TGA A TTT AGT CAC GAC GAG TCA TT A TTT AGT CAC GAC GAG TCA TT A TAGCTA
	Z-n2-B''	AGT ACG AAC GAC TGT ACG A TTT AGT CAC GAC GAG TCA TT A TTT AGT CAC GAC GAG TCA TT A TAGCTA
Dummy Links	X-n2-Dummy	GTA GGT AGG AAT AGT TGA A TTT AGT CAC GAC GAG TCA TT A TTT AGT CAC GAC GAG TCA TT
	Y-n2-Dummy	TTG CTG AGT ATG AGT GGA A TTT AGT CAC GAC GAG TCA TT A TTT AGT CAC GAC GAG TCA TT
	Z-n2-Dummy	AGT ACG AAC GAC TGT ACG A TTT AGT CAC GAC GAG TCA TT A TTT AGT CAC GAC GAG TCA TT
Dupl.	Duplexer d20	AAT GAC TCG TCG TGA CTA AA

All PAE designs used in this work are modifications of prior systems shown to form the desired crystal types being examined, and a complete description of the design parameters can be found in this prior work.¹ For the BCC system, X-n2-A and Y-n2-A' were used to produce two sets of particles that were complementary to each other. FCC structures were produced using a self-complementary linker design, X-n2-B''. The AlB₂ crystal structure was formed by using the same sticky ends as the BCC structure, but with two different linker lengths, X-n1-A and Y-n3-A' (n = 1 and n=3) and a specified ratio of linker strands between the two particle types that was known to produce AlB₂ structures.¹ Additionally, the AlB₂ structure required two different nanoparticle diameters to form the appropriate structures, so 10 nm particles were used in conjunction with the short linker (20 nm were still used for the other). A CsCl lattice was also made using the same nanoparticles and linkers but with the short DNA on the 20 nm nanoparticles and vice versa to create the same hydrodynamic radius for both particle types. Substrates were functionalized with

n=2 linkers complementary to the substrate anchor strand (Z-n2-** in table). To alter the substrate functionalization, ‘dummy’ linkers that did not have sticky ends were used in the appropriate ratio with the active strands.

Nominal 20 nm diameter gold nanoparticles were synthesized from an established seeded growth protocol.⁴ Briefly, a 500 mL solution of 2.2 mM trisodium citrate dihydrate was brought to a boil. 2 mL of 25 mM H_{AuCl}₄:3H₂O was

quickly injected to the solution under energetic stirring. After the initial injection to synthesize the seeds, the solution temperature was lowered to 90 °C and allowed to equilibrate for 30 minutes. Then another injection of 2 mL of 25 mM H_{AuCl}₄:3H₂O was added, the solution was allowed to equilibrate for an additional 30 minutes, and a final injection of another 2 mL of 25 mM H_{AuCl}₄:3H₂O was performed. The nanoparticles were characterized by casting onto formvar coated TEM grids, and the particle size distribution was calculated by imaging at least 250 nanoparticles. Analysis was performed with ImageJ (Supplementary Figure 2).



Supplementary Figure 2: 20 nm gold nanoparticle size distribution.

2. Nanoparticle Functionalization Procedure

Thiolated DNA functionalization of gold nanoparticles was performed using a variation of a previously described method.⁵ The thiolated DNA was suspended in 100 mM dithiothreitol (Sigma Aldrich) for one hour to cleave the 3' propyl-mercaptan protecting group, then desalted using a NAP5 size exclusion column (GE Healthcare). The deprotected DNA (either HS-X or HS-Y) was added to the colloidal gold nanoparticles in a molar ratio of ~6000:1 (roughly 20-fold excess of DNA). After a 1 hr incubation, enough 1 wt% sodium dodecyl sulfate (SDS) solution was added to bring the concentration to 0.01% and the solution was vortexed briefly, followed by the addition of a phosphate adjustment buffer (0.021 M NaH₂PO₄, 0.079 M Na₂HPO₄) to bring the solution to 10 mM phosphate. After vortexing and then allowing the solution to incubate for 30 minutes, six additions of 2 M NaCl, 10 mM phosphate buffered saline (2 M PBS) were added in half-hour increments (vortexed after each addition), until the final concentration of 0.5 M NaCl was reached. The solution was allowed to incubate overnight to ensure maximum DNA loading. To separate the

unbound DNA from the PAEs, the solution was aliquotted into 1.5 mL centrifuge tubes and three rounds of centrifugation (Eppendorf 5242, 12,000 rpm, 20 min) were performed. In between centrifugation steps, the supernatant was siphoned off and the nanoparticles resuspended by filling the Eppendorf tube with nanopure water (~1.4 mL). After the last round of centrifugation and supernatant removal, the remaining volume (~50-100 μ L) of DNA-nanoparticle solution was measured, and 2 M PBS was added to bring the NaCl concentration to 0.5 M. The concentrations of the resulting nanoparticle solutions were determined using absorbance at 520 nm measured on a Cary 50 UV-Vis-NIR spectrophotometer (Agilent) and known extinction coefficients.

Thiolated DNA functionalization of the gold-coated quartz substrates was done by incubating each substrate in a 1.5 mL centrifuge tube (Fisher Scientific) containing 5 μ M deprotected HS-Z DNA solution (0.5 M NaCl, 0.01% SDS, 10 mM phosphate buffered saline) overnight. The substrates were then washed five times in 0.5 M PBS to remove unbound DNA.

3. Linker Strand Preparation

Upon arrival, linkers and duplexers that were received from IDT were resuspended in nanopure water and aliquotted into 50 or 100 μ mol lots, then re-lyophilized for freezer storage. The lots of linkers and duplexers used for experiments were then resuspended in 100 μ L nanopure water, then a small amount measured in the UV-Vis to determine the concentration. 50 μ M duplexed linker stocks were prepared by adding Duplexer strands to Linker strands in a molar ratio of n:1, where n is the number of duplexer sections, adding 2 M PBS until the salt concentration reached 0.5 M, then diluting to the final PAE concentration in 0.5 M PBS. The linkers were heated to 35 $^{\circ}$ C for 1 hour to achieve full hybridization.

4. AFM Imaging

Selected substrates were imaged with an AFM (Bruker Dimension Fastscan, Icon head, SNL-10 8 nm radius tip), performed in the same salt concentration PBS that was used to produce the samples. Imaging crystals was extremely time consuming, as the height of the crystals required slow scan times and occasionally were too tall to image (the probe height was only ~5 μ m), so this was not performed at scale.

5. Silica Embedding Procedure

Initial experiments used a silica sol-gel process⁶ that has previously been demonstrated to adequately preserve the structure of PAE thin films when removed from solution. However, it was

found that the previously developed procedure did not fully embed the entirety of the large crystals (microscopy data suggested that the outside of the crystal was embedded, but the interior of the crystals was not fully encapsulated with silica, leading to the collapse of the crystal upon drying – see Supplementary Figure 11 for examples), and also occasionally left silica chunks stuck to the substrate that impeded analysis of the crystals. A modification of this prior silica embedding procedure was therefore developed in order to produce the images of the PAE superlattices in this work.

The optimized embedding procedure used the same chemicals as prior work, but modified the protocol slightly to improve the quality of the silica-embedded structures. 1.5 μL of *N*-trimethoxysilylpropyl-*N*, *N*, *N*-trimethylammonium chloride (TMSPA, Gelest, 50% in methanol) was added to the substrates submerged in 1 mL of 0.5 M PBS (note that this is not the same salt concentration as the depositions occurred in), and left on the thermomixer at 1400 rpm at room temperature overnight. Then 2 μL of triethoxysilane (TES, Sigma Aldrich) was added and samples left on the thermomixer for an additional 12-24 hrs. The samples were then rinsed by placing them in an Eppendorf tube in DI water and vortexing for 5-10 seconds, repeated 5x. After the fifth rinse, samples were placed in open Eppendorf tubes and allowed to air dry overnight before SEM imaging. The low concentrations and long times seem to allow the penetration of the chemicals without forming a silica crust on the surface of the crystals (which was seen with higher concentrations), and good SEM images were able to be taken with this new procedure.

Supplementary Note 1 - Equations and Analysis

1. *Crystal Growth from Surfaces*

The capillarity theory of heterogenous nucleation utilizes a simple model of a free energy change when an aggregate coalesces on the surface. This is simply the balance of the Gibbs free energy change, ΔG :

$$\Delta G = V\Delta G_v + A_{cf}\gamma_{cf} + A_{cs}\gamma_{cs} - A_{sf}\gamma_{sf} \quad (\text{eq S1})$$

where ΔG_v is the free energy change per unit volume, A_{cf} , A_{cs} and A_{sf} are the surface areas of the affected interfaces, where the subscripts c, f, and s refer to the crystal, fluid and substrate respectively, and γ_{cf} , γ_{cs} , γ_{sf} refer to the surface energies of those interfaces. A_{sf} and A_{cs} are necessarily equal, as the interface area lost by the substrate-fluid interface is equal to the interface

area gained by the crystal contacting the substrate. For a hemispherical droplet, the areas of those interfaces can be described simply by the radius and contact angle with the surface, such that $A_{cf} = 2\pi r(1-\cos\alpha)$ and $A_{sf} = A_{cs} = \pi r \sin^2\alpha$. The volume can also be described in terms of the contact angle, $V = \pi/3 (2-3\cos\alpha + \cos^3\alpha)$. With the hemispherical droplet assumption and an assumption of mechanical equilibrium in the horizontal directions, Young's equation can be derived (eq S2):

$$\gamma_{sf} = \gamma_{cs} + \gamma_{cf} \cos \alpha , \quad \text{or} \quad \cos \alpha = \frac{\gamma_{sf} - \gamma_{cs}}{\gamma_{cf}} \quad (\text{eq S2})$$

This equation illustrates that the contact angle of the droplet depends solely on the surface energies of the materials involved. If one utilizes the assumption of a hemispherical droplet, the change in Gibbs free energy upon nucleation can be used to determine a critical nucleus size required for the film material to remain stable on the surface. This critical nucleus size is

$$r^* = \frac{-2(2\pi\gamma_{cf}(1-\cos\alpha) + \pi\sin^2\alpha(\gamma_{cs} - \gamma_{sf}))}{\pi(2-3\cos\alpha + \cos^3\alpha)\Delta G_v} \quad (\text{eq S3})$$

The critical nucleus size has a corresponding ΔG_v^* , which is used to determine the density of stable nuclei on the surface:

$$N^* = n_s \exp\left(\frac{-\Delta G_v^*}{k_B T}\right) \quad (\text{eq S4})$$

However, to capture the effect of surface coverage on crystallization kinetics, a 2D JMAK model can be utilized with nucleation rate \dot{N} and growth rate \dot{G} :

$$\dot{N} = \dot{N}_0 e^{-\frac{\Delta G_N}{kT}} \theta^{n^*} \quad (\text{eq S5})$$

$$\dot{G} = \dot{G}_0 e^{-\frac{\Delta G_G}{kT}} \theta \quad (\text{eq S6})$$

where it is assumed that nucleation proceeds by a reaction of n^* surface nanoparticles to form a stable cluster, while growth proceeds by first-order reaction of surface nanoparticles to the crystal. Here, θ is the fractional surface coverage. Nucleation density is then given by:

$$N^* = \frac{1}{X^3} = \frac{\dot{N}}{\dot{G}} = \frac{\dot{N}_0}{\dot{G}_0} e^{-\frac{(\Delta G_N - \Delta G_G)}{kT}} \theta^{n^*-1} \quad (\text{eq S7})$$

For the equation to converge to the thermodynamic limit, the Arrhenius constants must reduce to:

$$N^* = n_s e^{\frac{-\Delta G}{kT}} \theta^{n^*-1} \quad (\text{eq S8})$$

Using a quasi-static approximation, the surface coverage can be estimated by its equilibrium surface coverage as a function of free nanoparticle concentration in solution (c) and adsorption equilibrium constant (K):

$$\theta = \frac{Kc}{1+Kc} \rightarrow 1 \text{ for } Kc \gg 1 \quad (\text{eq S9})$$

Literature values for the equilibrium constant of PAEs adsorbing to substrates at 40 °C is given to be $K \sim 1.8 * 10^3 \text{ nM}^{-1}$.⁷ Because a monolayer is stable at higher temperatures than those at which crystallization occurs,⁸ crystallization in solution prior to total surface adsorption can be neglected, and the concentration of free nanoparticles in solution (c) can be approximated by the starting concentration of nanoparticles in solution: 10 nM, 20 nM, 50 nM. Under these assumptions, the value of Kc may be estimated as $Kc \approx 1.8 * 10^4, 3.6 * 10^4, 9.0 * 10^4 \gg 1$ for all experiments in this study. Therefore, at all concentrations used for this analysis, the film is expected to achieve total surface coverage, and therefore the nucleation density is anticipated to be independent of the concentrations used.

In the absence of known quantities for $\Delta G_v, \gamma_{cf}, \gamma_{cs}, \gamma_{sf}$ in each PAE system, the nucleation density of crystals on a surface may be quantitatively estimated by the size of the nucleation exclusion zone surrounding the crystallite:⁹

$$N^* \sim \frac{1}{D_{SD} \tau_s} = a_0^2 e^{\frac{-\Delta H_{des} - \Delta H_{dif}}{kT}} \rightarrow a_0^2 e^{\frac{-\Delta H_{des}}{kT}} \quad (\text{eq S10})$$

where D_{SD} is the surface diffusivity of the nanoparticle. τ_s is the residence time on the surface, a_0 is the spacing between surface attachment sites (estimated by the spacing of the DNA graft at the surface), ΔH_{des} is the enthalpy barrier for desorption from the surface (estimated by the enthalpy of one DNA-DNA bond between nanoparticle and surface), and ΔH_{dif} is the enthalpy barrier for diffusion (assumed to be much smaller than ΔH_{des}).

2. *Density of Nuclei on Surface*

The Arrhenius form of the nucleation density indicates that the process is dependent on parameters such as the DNA-DNA binding energy, which may be modulated by salt concentration, as well as the temperature, which may be controlled externally. In principle, crystallization could occur at all

stages of the slow-cooling process, resulting in a complicated dynamic system as the rate of crystallization and concentration of free nanoparticles changes with time. However, crystallization is suppressed above the melting temperature due to a lack of driving force, and is suppressed below the melting temperature due to the depletion of free nanoparticles, resulting in crystallization occurring in a small window around the melting temperature. Therefore, the crystallization process can be approximated as occurring exclusively at the melting temperature, which simplifies this kinetic analysis to a single temperature of interest:

$$\int_0^t \frac{d}{dt} N(T(t), t) dt \approx N(T_m) \quad (\text{eq S11})$$

The effect of salt concentration (c_{salt}) on the DNA-DNA binding energy is also captured in this assumption, due to the proportional relation between enthalpy and temperature at the transition point

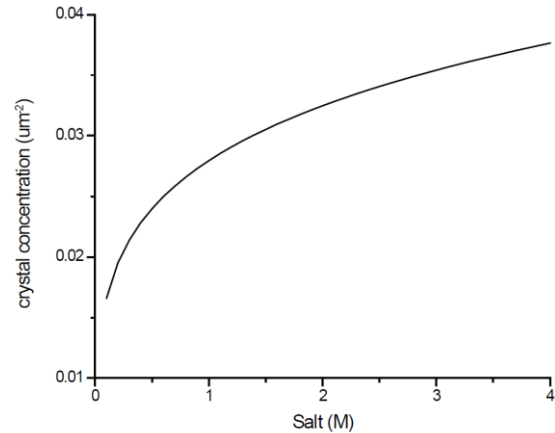
$$T_m(c_{salt}) = \frac{\Delta H(c_{salt})}{\Delta S} \quad (\text{eq S12})$$

where ΔH , and therefore T_m , increases with salt concentration due to screening the repulsive Coulombic interaction between the negatively charged DNA. Empirically, this trend has the logarithmic form:¹⁰

$$T_m(c_{salt}) = a + b \text{Log} \left(\frac{c_{salt}}{c_0} \right) \quad (\text{eq S13})$$

With fit parameters $a, b > 0$ and reference concentration c_0 , where $a = 51$ °C, $b = 10$ °C, and $c_0 = 1$ M (Supplementary Figure 3). Therefore, the nucleation density increases with concentration c_{salt} according to:

$$N^* \sim a_0^2 e^{-\frac{\Delta H_{des}}{k \left(a + b \text{Log} \left(\frac{c_{salt}}{c_0} \right) \right)}} \quad (\text{eq S14})$$



Supplementary Figure 3: Nucleation density vs. NaCl concentration.

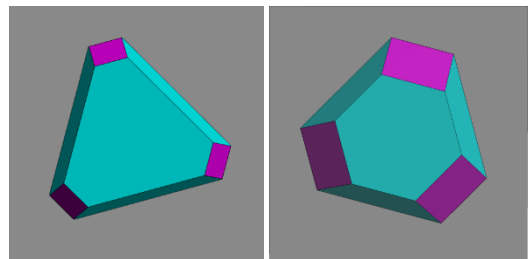
3. Winterbottom Construction Calculations

BCC:

BCC crystals (in both orientations explored in this work) are truncated by $\{110\}$ facets, as those facets have the lowest surface energy¹¹. In prior work, the calculated ratio (both from a broken bond model and MD simulations) of surface energies of the facets, $\gamma_{110} : \gamma_{111} : \gamma_{100}$ range from 1:1.22:1.41 for a 24-base DNA linker to 1:1.76:1.36 for a 96-base DNA linker. Regardless, the $\{110\}$ facets have significantly lower energy than the other two, resulting in Wulff constructions that are entirely bound by those facets. The first set of values was used in the freely available software, WulffMaker: Winterbottom shapes v3.0¹² to confirm the equilibrium shapes and determine the surface energy ratio between the substrate and the $\{110\}$ facets. For the $\langle 100 \rangle$ orientation, in order to form the pyramidal structure with only four sides, the relative difference in surface energy between the substrate-crystal interface and the substrate-vapor interface, $\gamma_{cf} - \gamma_{sf}$, must be less than -0.7 (note this is a normalized value assuming a normalized $\gamma_{110} = 1$). Below that threshold, all ratios produce the pyramidal structure observed in the experimental data, so the exact value of $\gamma_{cf} - \gamma_{sf}$ cannot be determined. For the $\langle 110 \rangle$ orientation, however, the relative height of the crystal compared to its top face yields a more accurate estimate of the surface energy, which was determined to be approximately -0.25 for the AFM imaged sample. Because the surface is bi-functionalized in the $\{110\}$ case, it is to be expected that the surface energy difference would be less than half that of the mono-functionalized case, as individual PAEs on a $\{110\}$ surface will interact with both complementary and non-complementary DNA. Because DNA is negatively charged, interactions between non-complementary DNA strands are repulsive; changing the complementary sequence to non-complementary results in the removal of attractive forces, and an increase in the surface energy of the substrate-crystal interface (thereby decreasing the surface energy difference $\gamma_{cs} - \gamma_{sf}$).

FCC:

Using the WulffMaker software, surface energies were adjusted until the shape matched experiments. It was found that for this system, the visible facets had relative surface energies of $\gamma_{111} : \gamma_{100}$ of 1:1.4, with γ_{110} being at least 1.22. (For a different FCC linker design, previous work¹¹ predicted the ratio of $\gamma_{110} : \gamma_{111} : \gamma_{100}$ surface

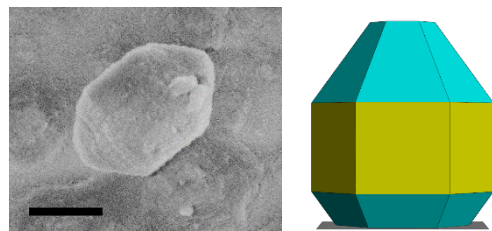


Supplementary Figure 4: Winterbottom Shapes for FCC with different surface energy ratios. Left - $\gamma_{111} : \gamma_{100} = 1:1.4$, Right - $\gamma_{111} : \gamma_{100} = 1:1.22$.

energies to be 1:1.15:1.22, however these values create a much larger (100) surface (purple in Supplementary Figure 4) than was observed in either the Winterbottom shape or the solution-phase crystals seen in Supplementary Figure 17.)

AlB₂:

The AlB₂ hexagonal structure has a point group of -6m2; using WulffMaker software, the predicted structure on a (0001) surface for three facet families is a hexagonal pyramid bound by {111} facets and truncated on top by a (100) facet (See Figure 5). From previous work,¹ the crystal should have a c/a ratio of ~0.8 for the linker design used here. The surface energy ratios were estimated from a single image of a Wulff polyhedra in solution



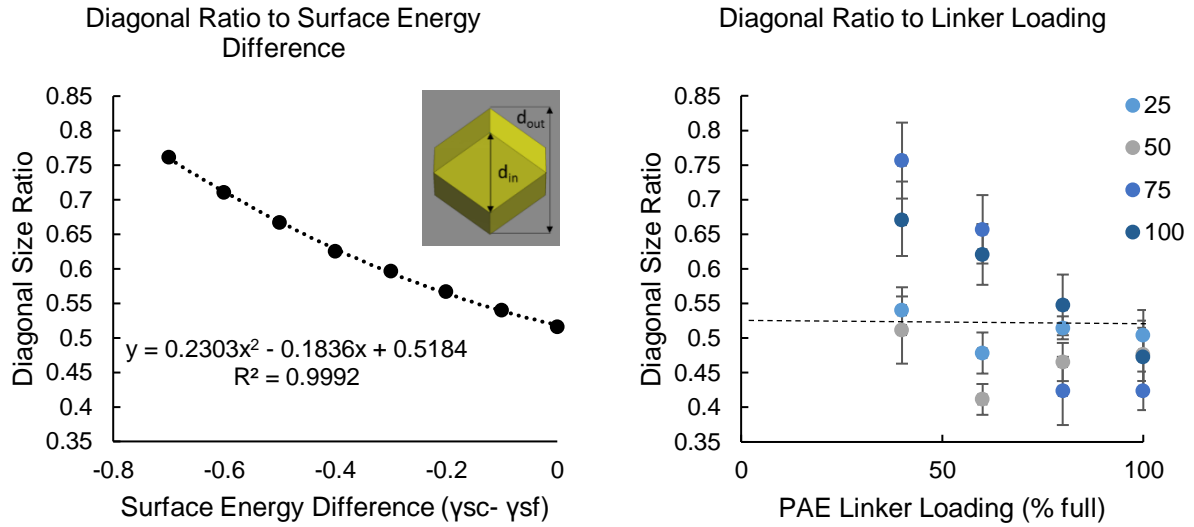
Supplementary Figure 5: AlB₂ surface energy ratio calculated from adjusting shape from WulffMaker software (right) to match crystal from experiment (left). Scale bar is 2 μ m.

(Supplementary Figure 5), resulting in $\gamma_{110} : \gamma_{111} : \gamma_{100} = 1 : 1.15 : 1.6$. Note, surface-bound crystals on surface did not show the (110) plane, which could have resulted in any value for the ratio.

4. Analysis of Winterbottom Shape Change with Linker Density

As shown in Figure 3, the {110} facets that are perpendicular to the substrate shrink as the surface energy difference becomes more negative and the crystal ‘sinks’ into the substrate. The size of the short diagonal across the top vs. across the bottom of the crystal was measured from those images to generate a plot of relative size versus surface energy difference (Supplementary Figure 6). While in principle the ratio of these two values could be used to determine the relative differences in surface energies for the Winterbottom constructions, the silica embedding process that is required to image the samples causes the lattice parameter of PAE crystals to shrink. When affixed to a substrate, the particles at the bottom of a crystal are pinned in place by the DNA connections that bind the PAEs to the substrate.¹³ As a result, the PAE Winterbottom constructions are expected to shrink more at the top of the crystal than at the bottom. Thus, for very tall crystals that are well adhered to the substrate (i.e. for a surface energy difference of zero), the size ratio will be well below the predicted value because the top of the crystal is able to shrink significantly more than the bottom of the crystal upon silica embedding. Conversely, when crystals have a low affinity for the surface (surface energy difference >0) the crystal will sit more atop the substrate and shrinkage

will be more isotropic, leading to size ratios near predictions (0.5184). Therefore, only qualitative trends can be determined from this analysis (Supplementary Figure 6).



Supplementary Figure 6: Left - Diagonal ratio to surface energy difference from Winterbottom construction. Right – Diagonal ratio to linker loading (colors are % active strands on the surface). Values of diagonal size ratio below 0.518 do not represent meaningful information, as these values should not be possible in a Winterbottom construction. These low values are influenced by the silica-embedding induced shrinkage, indicating that they cannot be used on their own to accurately confirm the exact aspect ratios or surface energies of these crystals. Nevertheless, the qualitative trends are consistent with the expected changes to Winterbottom construction shape based on the analysis presented here. Error bars correspond to one standard deviation with minimum of five experimental replicates.

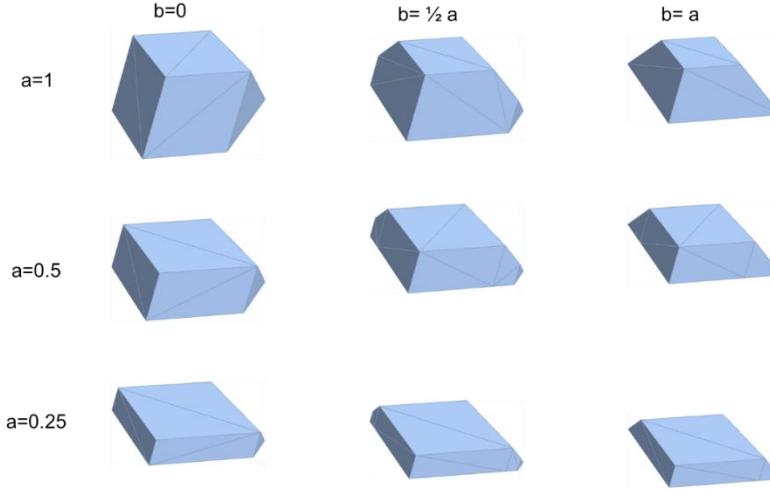
5. Deviations from Winterbottom Construction Predicted Shape

To investigate the transition between the thermodynamically predicted Winterbottom configuration, and the observed “diamond-like” configuration, a 2-variable parameterization was utilized to describe the shape of the crystal polyhedra. The first parameter “a” ($0 < a < 1$) describes the height of the crystal from the surface, where $a=1$ corresponds to a bisected Wulff polyhedra, and $a=0$ corresponds to a perfectly wetting material. The second parameter “b” ($0 < b < a$) corresponds to the length of the non-Winterbottom protrusion, where $b=0$ corresponds to the flat edge observed in the Winterbottom construction, and $b=a$ corresponds to a sharp point. The non-normalized geometry has parameterized points corresponding to:

$$\left\{0, \frac{1}{2}, \frac{1}{\sqrt{2}}\right\}, \left\{0, -\frac{1}{2}, \frac{1}{\sqrt{2}}\right\}, \left\{\frac{1}{\sqrt{2}}, 0, \frac{1}{\sqrt{2}}\right\}, \left\{-\frac{1}{\sqrt{2}}, 0, \frac{1}{\sqrt{2}}\right\}, \left\{0, \frac{1+a}{2}, \frac{1-a}{\sqrt{2}}\right\}, \left\{0, \frac{1}{2}(1-a), \frac{a-1}{\sqrt{2}}\right\}, \left\{\frac{1}{\sqrt{2}}, \frac{a}{2}, \frac{1-a}{\sqrt{2}}\right\},$$

$$\left\{\frac{1}{\sqrt{2}}, -\frac{a}{2}, \frac{1-a}{\sqrt{2}}\right\}, \left\{-\frac{1}{\sqrt{2}}, \frac{a}{2}, \frac{1-a}{\sqrt{2}}\right\}, \left\{-\frac{1}{\sqrt{2}}, -\frac{a}{2}, \frac{1-a}{\sqrt{2}}\right\}, \left\{\frac{1+b}{\sqrt{2}}, \frac{a-b}{2}, \frac{1-a}{\sqrt{2}}\right\}, \left\{\frac{1+b}{\sqrt{2}}, \frac{1}{2}(b-a), \frac{1-a}{\sqrt{2}}\right\},$$

$$\left\{-\frac{1+b}{\sqrt{2}}, \frac{a-b}{2}, \frac{1-a}{\sqrt{2}}\right\}, \left\{-\frac{1+b}{\sqrt{2}}, \frac{1}{2}(b-a), \frac{1-a}{\sqrt{2}}\right\}, \left\{\frac{1+b}{\sqrt{2}}, 0, \frac{1-b}{\sqrt{2}}\right\}, \left\{-\frac{1+b}{\sqrt{2}}, 0, \frac{1-b}{\sqrt{2}}\right\}$$



Supplementary Figure 7: Shape change as a function of crystal height from surface (a) and pointiness (b).

The volume of the convex hull defined by the parameterized points was calculated via triangulation

$$\text{Parameterized Volume} = \frac{1}{6}(b^3 + 3a^2(1 + b) + 3a(1 - b^2)) \quad (\text{eq S15})$$

The growth of each face due to surface diffusion is assumed to be proportional to length of the edge in contact with the surface (where particles from the surface attach to the face) divided by the area of the face (which must be filled before the next layer of particles can form).

This face area/edge ratio for the pointed face, normalized to unit volume, is calculated to be:

$$\text{Ratio for pointed face} = \frac{2^{7/6} \left(a - ab^2 + \frac{b^3}{3} + a^2(1+b) \right)^{1/3}}{a-b} \quad (\text{eq S16})$$

This face area/edge ratio for the side face, normalized to unit volume, is calculated to be:

$$\text{Ratio for side face} = \frac{6^{1/6}(1+b)(b^3+3a^2(1+b)-3a(-1+b^2))^{1/3}}{-b^2+2a(1+b)} \quad (\text{eq S17})$$

Therefore, the relative growth rate of the side face relative to the pointed face may be estimated by the ratio of these two values:

$$\text{Relative growth rate} \approx \frac{\sqrt{3}(a-b)(1+b)}{-2b^2+4a(1+b)} \quad (\text{eq S18})$$

When the relative growth rate is less than one, the point face grows faster than the side face, causing the structure's "point" feature to grow faster. Evaluating for $0 < a < 1$ and $0 < b < a$,

the relative growth rate never exceeds $\frac{\sqrt{3}}{4}$ (~ 0.43), which indicates that the “point” feature is kinetically preferred. Furthermore, as the crystal shape deviates further from the thermodynamically preferred Winterbottom construction, the face’s edge/area ratio also increases, further favoring the growth of the “point” feature.

The area of the crystal/liquid medium interface normalized to unit volume (A_{cf}) is calculated to be:

$$A_{cf} = \frac{2^{1/6}(1+a^2-b^2+2a(2+b))}{(a-ab^2+\frac{b^3}{3}+a^2(1+b))^{2/3}} \quad (\text{eq S19})$$

and the area between the crystal and the substrate normalized to unit volume A_{cs} is calculated to be:

$$A_{cs} = \frac{2^{1/6}(1+2a-b)(1+b)}{(a-ab^2+\frac{b^3}{3}+a^2(1+b))^{2/3}} \quad (\text{eq S20})$$

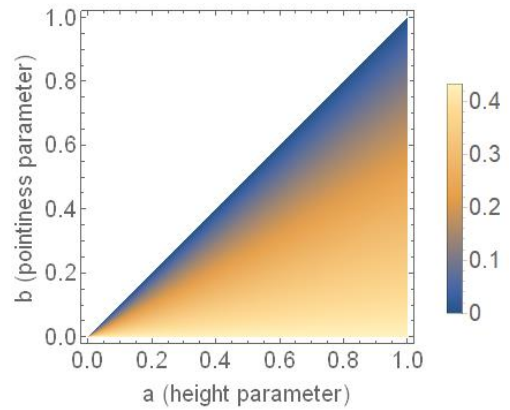
The free energy of a crystal was calculated from the surface energies of the crystal-substrate, crystal-liquid, and liquid-substrate interfaces.

$$E = \gamma_{cf} * A_{cf} + (\gamma_{cs} - \gamma_{fs}) * A_{cs} \quad (\text{eq S21})$$

This free energy is minimized when $a = 1 + \frac{\gamma_{cs}-\gamma_{fs}}{\gamma_{cf}}$, where $-1 < \frac{\gamma_{cs}-\gamma_{fs}}{\gamma_{cf}} < 0$

The difference in energy between the thermodynamically preferred Winterbottom structure and the kinetic structure, which corresponds to the driving force for rearrangement, is therefore calculated as:

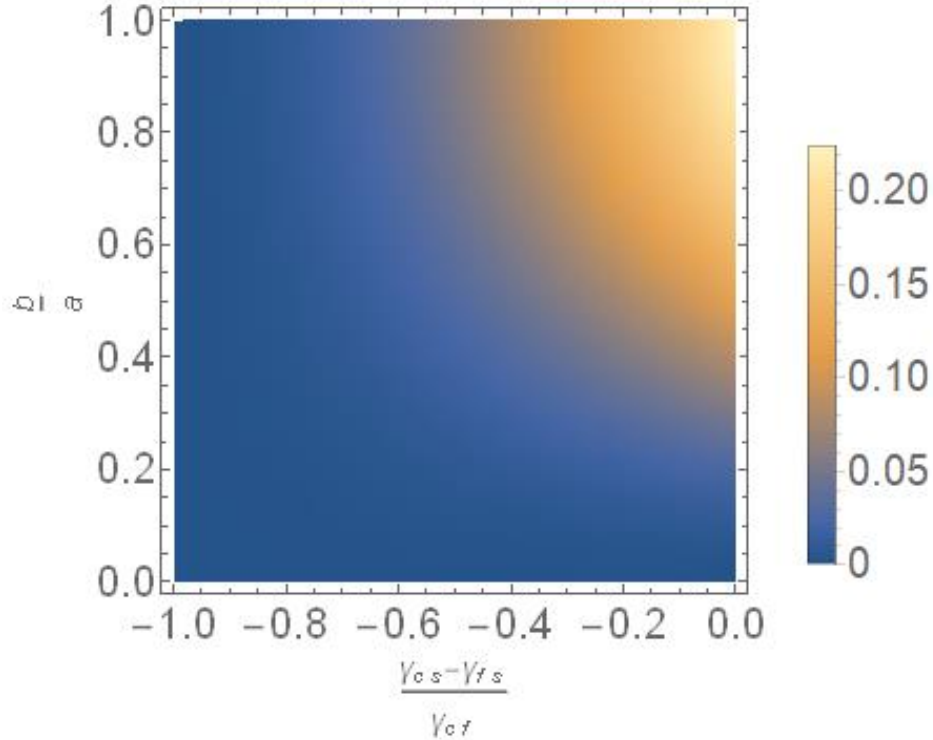
$$\begin{aligned} \Delta E(a, b) &= E(a, b) - E(a, 0) \\ &= \gamma_{cf} * (A_{cf}(a, b) - A_{cf}(a, 0)) + (\gamma_{cs} - \gamma_{fs}) \\ &\quad * (A_{fs}(a, b) - A_{fs}(a, 0)) \end{aligned} \quad (\text{eq S22})$$



Supplementary Figure 8: Relative growth rate of point face to side faces for different pointiness and height values. In this construction, $b=a$ corresponds to a sharp point.

Utilizing the relation $a = 1 + \frac{\gamma_{cs} - \gamma_{fs}}{\gamma_{cf}}$, the thermodynamic driving force can be evaluated, normalized to the crystal-liquid surface energy as a function of the non-dimensionalized interfacial energy term $s = \frac{\gamma_{cs} - \gamma_{fs}}{\gamma_{cf}}$ and pointiness term $x = \frac{b}{a}$:

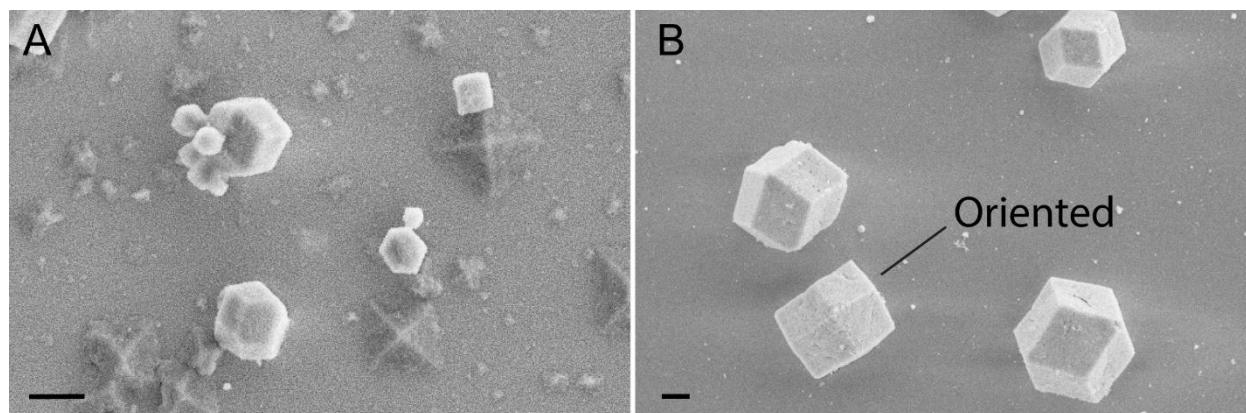
$$\frac{\Delta E}{\gamma_{XL} * V^{\frac{2}{3}}} = 2^{1/6} 3^{2/3} (1 + s) \left(\frac{3(2+s) - (1+s)^2(-2+x)x}{(3(1+s)(2+s) + 3(1+s)^3x - 3(1+s)^3x^2 + (1+s)^3x^3)^{2/3}} - \frac{3^{1/3}(2+s)}{((1+s)(2+s))^{2/3}} \right) \text{ (eq S23)}$$



Supplementary Figure 9: Normalized total surface energy difference relative to Winterbottom structure for crystals of different pointiness and normalized surface energy difference.

6. Crystals Depositing from Solution

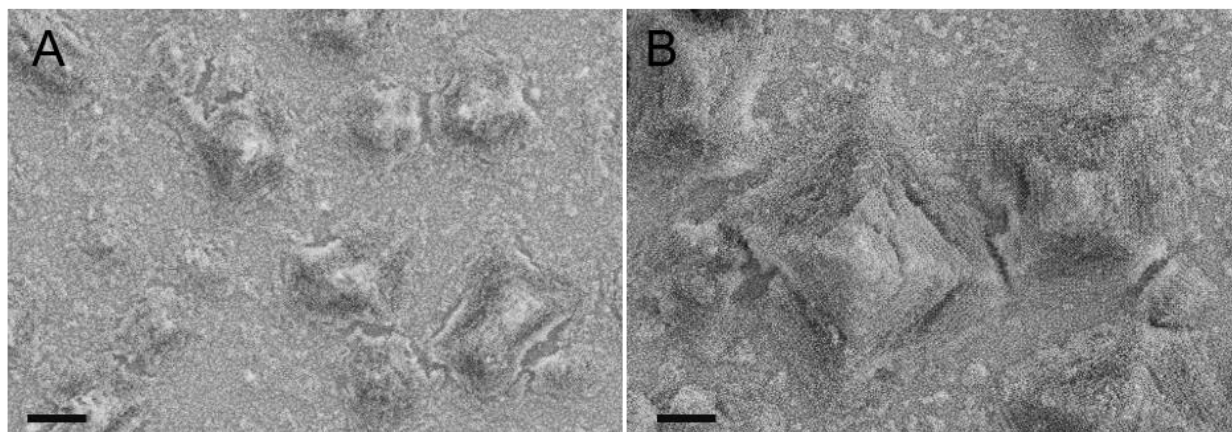
Crystals also form in solution during the slow cooling process, and can occasionally deposit on the substrate and adhere well enough to survive the silica embedding procedure. Crystals that have formed in solution and subsequently adhered to the substrate are readily identified in SEM imaging, as they charge more and have more contrast in SEM images due to having less contact with the substrate (Supplementary Figure 10A). On substrates where crystals have low affinity for the surface, identification of substrate-grown vs. solution-grown crystals is more difficult, but crystals that are observed to adhere in orientations that would not result in a large number of DNA connections to the substrate are hypothesized to likely have deposited from solution. Crystals that are aligned in the expected orientation but do not match the Winterbottom shape are rare, but cannot be positively identified as either solution- or substrate-grown and were thus not included in the analyses in the main text.



Supplementary Figure 10: (A) Crystals deposited from solution appear brighter in SEM imaging due to charging, and can be easily identified against crystals with a high affinity for the surface. (B). On substrates where crystals have a low affinity for the surface, identification of solution-grown crystals relies on them being unoriented to the substrate. Ones that are correctly oriented (in these images the surface is mono-functionalized, so the square point would be up if grown from the substrate) but do not have the same crystal shape as the majority of the observed surface-grown crystals cannot be determined to be solution or substrate grown to complete certainty and thus are omitted from analysis.

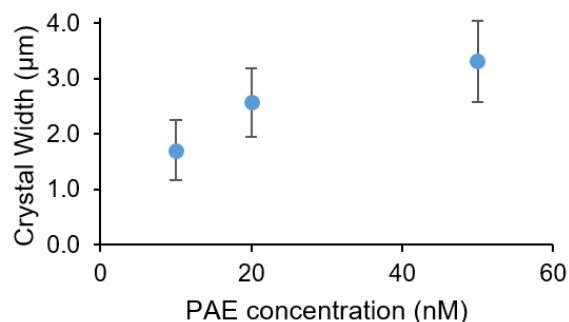
Supplementary Note 2- Additional Experiments

1. Crystal Size



Supplementary Figure 11: Increased PAE concentration results in larger crystals. {100} crystals, A) 10 nM, B) 50 nM. Scale bars are 1 μm .

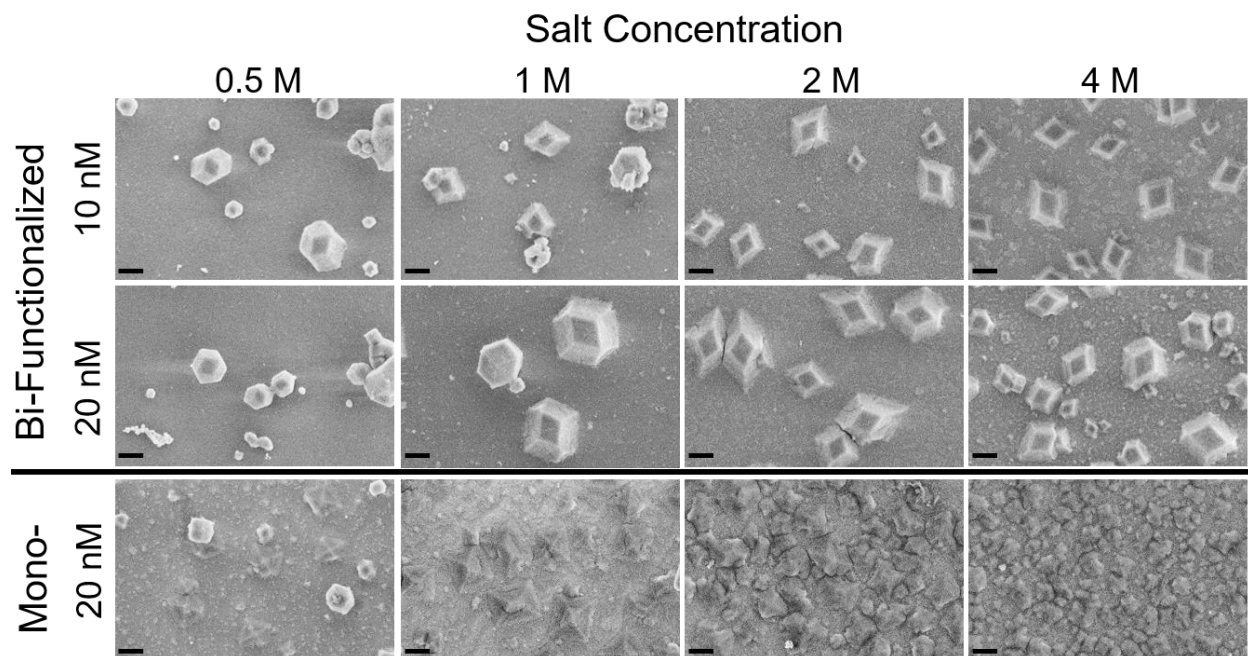
The effect of PAE concentration on the size of crystals was studied in 0.5 M PBS for both mono-functionalized and bi-functionalized surfaces. Concentrations of 10, 20, and 50 nM were studied for each substrate functionalization type. The bi-functionalized {110} surface did not show crystals that were identifiably grown on the surface, however some solution-phase crystals had deposited via sedimentation. The mono-functionalized surface showed an increase in size of the crystals with PAE concentration (Supplementary Figures 11 and 12), but the areal density (number/surface area) of crystals remained approximately constant between the PAE concentrations.



Supplementary Figure 12: Effect of PAE concentration on resulting crystal size in $\langle 100 \rangle$ oriented crystals. Error bars correspond to one standard deviation with a minimum of five experimental replicates.

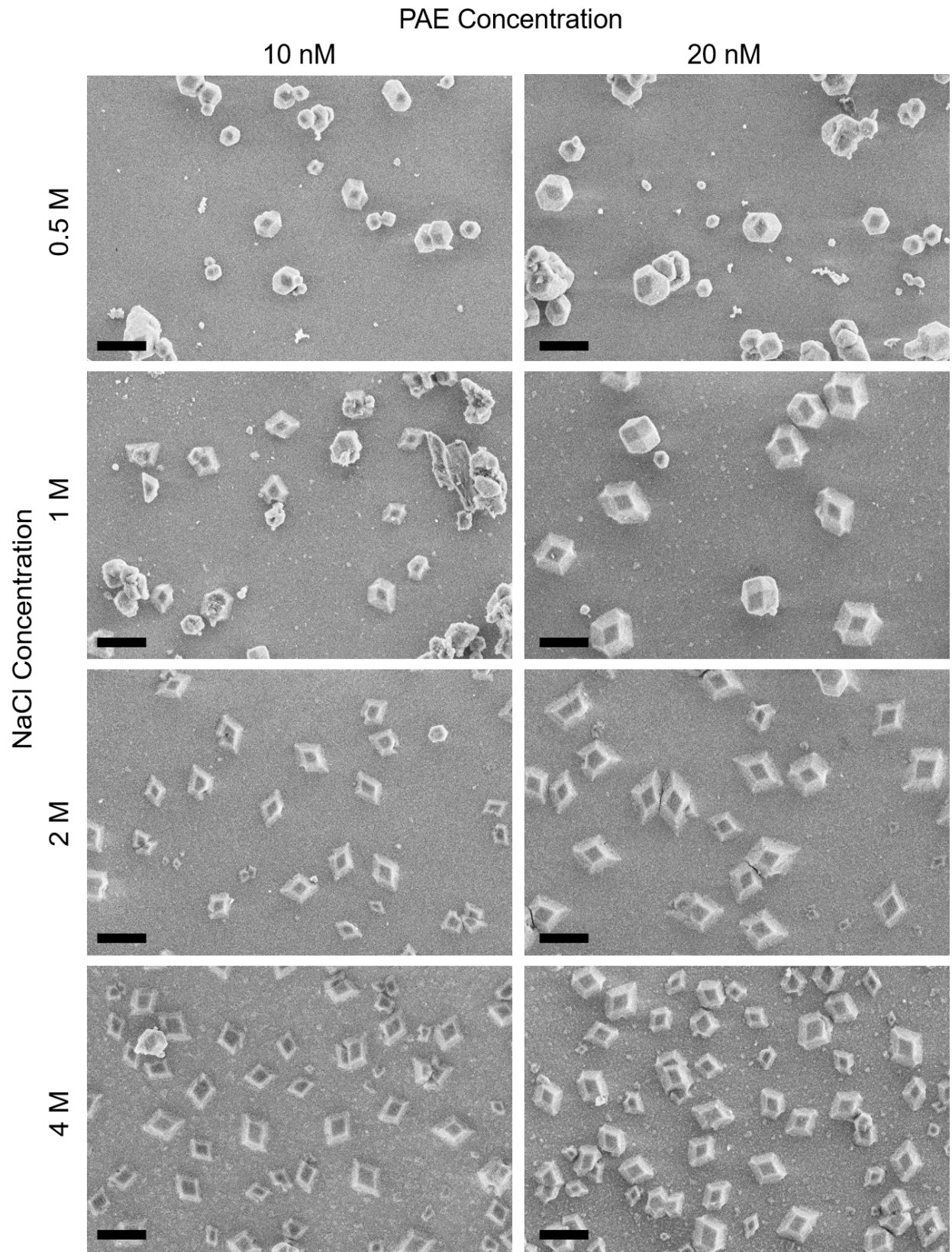
2. Salt Concentration

In addition to the bifunctionalized surface results described in the main text, salt concentration was also varied for the monofunctionalized substrates, and exhibited the same trends as noted for the bifunctionalized substrates (Supplementary Figure 13).



Supplementary Figure 13: Effect of salt concentration on crystal formation for both bi-functionalized and mono-functionalized surfaces (two different nanoparticle concentrations shown for bi-functionalized). As salt concentration is increased, more crystals nucleate and grow. For increased nanoparticle concentration, the size of the crystals becomes larger. Scale bars are 2 μm .

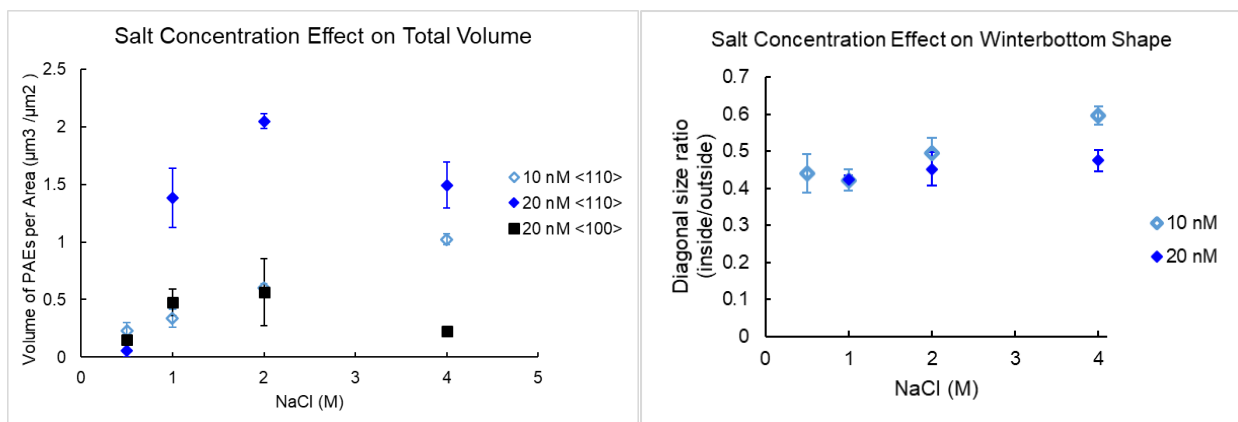
At higher salt concentrations (above 1M NaCl), the width of nanoparticles decreased, as noted in the main text. However, when the total number of deposited PAEs is estimated for each sample (calculated as average PAE crystallite volume times the areal density of crystals on the surface), the total number of PAEs on the surface was observed to increase with increasing NaCl concentration across the range studied for the 10 nM PAE samples; the 20 nM PAE samples showed the same relationship up to 2 M NaCl, with a slight decrease in number of PAEs deposited when going from 2 M to 4 M NaCl. However, these calculations do not include the significant number of nanoparticles that can be seen on the surface (outside of crystals) for the higher salt concentrations, providing one possible explanation for this decrease at 4M NaCl (a reduced amount of PAEs available for crystal growth due to adsorption of PAEs to the substrate that are not part of a crystallite). In addition, the shape of these crystallites was analyzed to determine if the overall height of the crystal was changing independent of width, as this would also affect the



Supplementary Figure 14: Representative images used for Figure 2 graph data. Scale bars are 5 μm

calculations of the number of PAEs deposited that were mentioned above. Results presented in Supplementary Figure 15 show that there is not a statistically significant change in Winterbottom shape for the 20 nM PAE samples, but shows slightly shorter crystals (higher crystal surface energy relative to substrate) for the 10 nM PAE samples at 4 M NaCl. Presuming similar DNA loading on the nanoparticles and substrate, it is not expected that the Winterbottom construction should change with NaCl concentration. Even though the total surface energy of both PAEs and substrate are changed as a function of NaCl concentration, they should change in the same ratio, and therefore the relative surface energies would be constant.

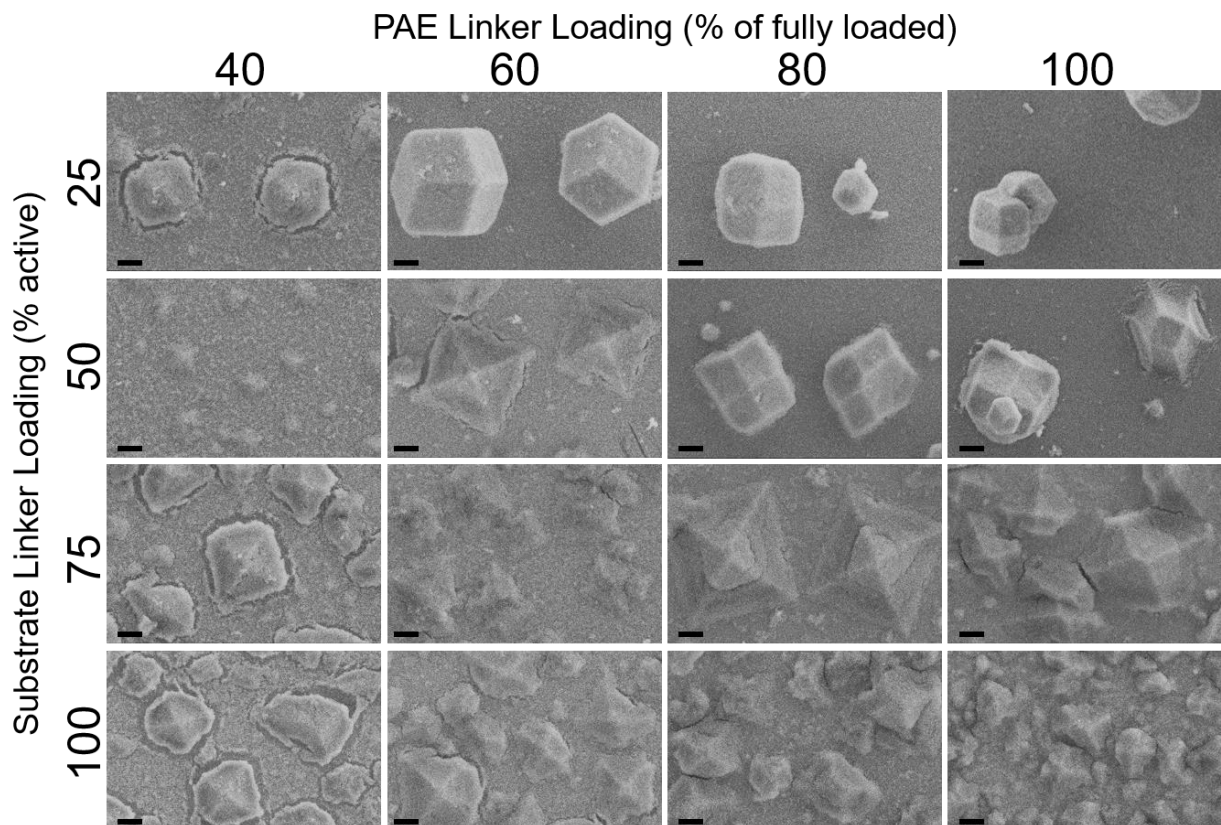
In order to further explain the trends in PAE deposition as a function of NaCl concentration, it is also important to note that at higher salt concentrations, complex interactions between the polyanionic PAEs are hypothesized to alter the surface potentials in a manner that could also result in crystal size reduction at high [PAE] and [NaCl]. These interactions include repulsion due to underscreening,¹⁴ depletion attractions,¹⁵ and surface-charge interactions.¹⁶ The results discussed in this section may indicate that more complex interactions may be occurring at the highest NaCl and PAE concentration, which may warrant future study.^{16,17}



Supplementary Figure 15: Left – As salt concentration increases, the total volume of nanoparticles adhered to the surface increases up to 2 M, then decreases for 20 nM concentrations for both <110> and <100> oriented films (note, calculation does not include PAEs not part of a crystal – at 4M salt, this omission underpredicts the total volume of PAEs on the surface). Right – Salt concentration has little effect on the Winterbottom shape for 20 nM PAE concentration, however may have an increasing trend for the 10 nM case. Error bars correspond to one standard deviation with minimum of five experimental replicates.

3. Linker Density Exploration with FCC and $\langle 100 \rangle$ BCC

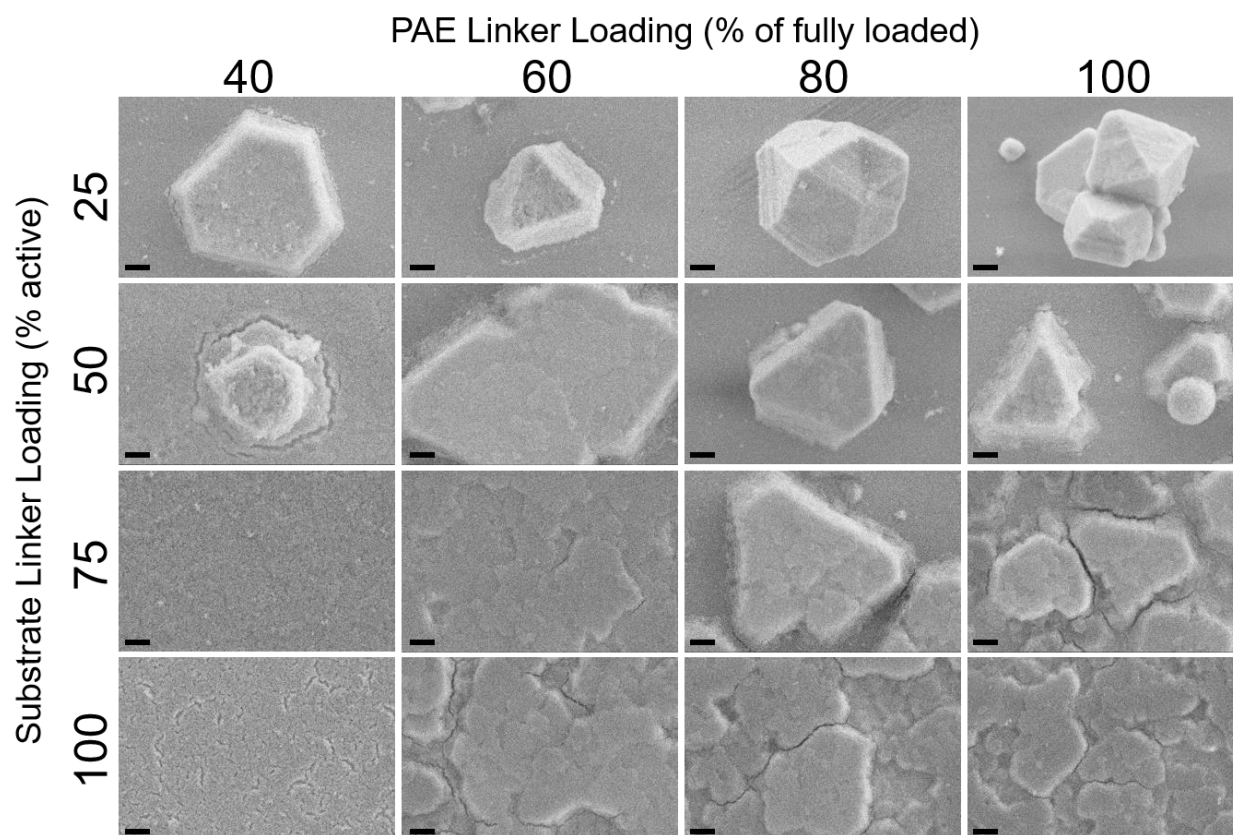
Monofunctionalized surfaces that produce $\langle 100 \rangle$ crystals were also tested with different linker loadings on the substrate and nanoparticles (Supplementary Figure 16). The same trends are demonstrated with the monofunctionalized substrates as observed in the bifunctionalized surfaces in the main text.



Supplementary Figure 16: Effect of linker loadings on crystal morphology, $\langle 100 \rangle$ orientation. Note that 25% linker loading with 60, 80, and 100% PAE loading did not show any crystals that could be identified as growing from the surface, crystals shown were deposited from solution. Scale bars are 1 μm .

Modification of crystal size and shape through alteration of the linker densities on the substrate and PAEs was also performed with the FCC system (Supplementary Figure 17). The same trend appeared as for the BCC systems, where increasing linker loading on the particles or decreasing substrate linker loading increased the height of the crystals relative to the lateral size. Interestingly, for the FCC system, a substrate linker loading of 100% with 40% linker loading on the PAEs produced flat, polycrystalline multilayer films. It is hypothesized that due to the increased affinity of the (111) plane to the surface (from hexagonal packing rather than square in the BCC system), the 100% linker loading was able to create flat films. Additionally, 75% substrate loading with 40% PAE linker loading also created flat multilayer films, however the grain size was very small,

indicating that crystal domain sizes within the flat films could potentially be tuned with further optimization.

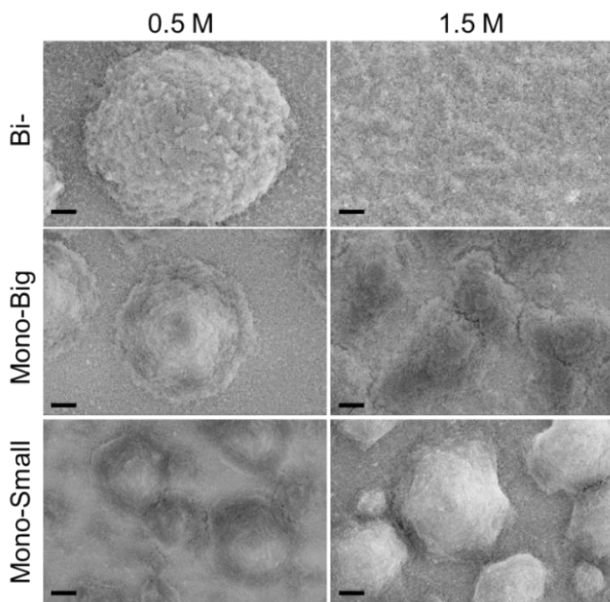


Supplementary Figure 17: Effect of linker density on crystal formation, FCC $\langle 111 \rangle$ orientation. Note that the 25% substrate linker loading with 80% and 100% PAE loading are crystals formed in solution; no crystals were observed to have formed on the substrate. Scale bars are 1 μm .

4. *AlB₂ experiments*

AlB₂ crystals were synthesized using PAEs with two different nanoparticle core sizes, specifically PAEs with nominally 10 nm (termed small) and 20 nm (termed big) nanoparticle cores. The small particle was functionalized with shorter X-n1-A linkers (one 20-base duplexer section), while the big particle was functionalized with longer Y-n3-A' (three 20-base duplexer sections) linkers. This size ratio has previously been reported to generate the predicted *AlB₂* structures.¹ At

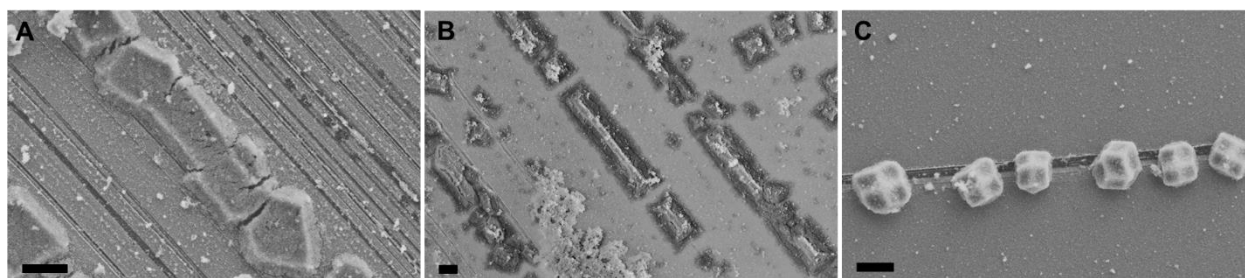
80% loading (ratio of DNA linker strands per thiolated DNA strands) on each nanoparticle type, the linker ratio between the large and small PAE is 2.6:1. To adjust closer to the 3:1 linker ratio in prior work,¹ the large particle was functionalized with 100% linker loading to produce a 3.2:1 ratio. Additionally, because there are two sizes of PAEs, it was hypothesized that the equilibrium structure may be different depending on whether the substrate was functionalized with DNA that was complementary to the big particle, the small particle, or both.¹³ Therefore, *AlB₂* crystals were grown on the three different substrate functionalizations. Because the *AlB₂* crystal structure has two different DNA lengths, growth in 1.5 M PBS rather than the 0.5 M PBS used in prior work could result in a slightly different crystal structure and affect the resulting Winterbottom constructions. Results for all six conditions are shown in Supplementary Figure 18. For 0.5 M PBS, both the monofunctionalized surfaces showed faceted hexagonal pyramids, as predicted by the Winterbottom construction. The bi-functionalized surface resulted in mounds with no discernable facets for the 0.5 M PBS. The 1.5 M PBS still resulted in faceted crystals on the monofunctionalized surfaces, however at the higher salt concentration there were significantly more crystals that impinged on one another, making the Winterbottom shape difficult to discern on the substrate functionalized complementary to the big particle. At the higher salt concentration, the bi-functionalized surface resulted in a film rather than individual mounds; it is hypothesized that this is a result of significantly higher nucleation density at higher salt concentration.



Supplementary Figure 18: *AlB₂* structures grown in two different salt concentrations and three different substrate functionalizations (mono-functionalized with the substrate complementary to either the big or small particle, and bi-functionalized). Scale bars are 1 μm .

5. *Nucleation of Single Crystals at Surface Defect Sites*

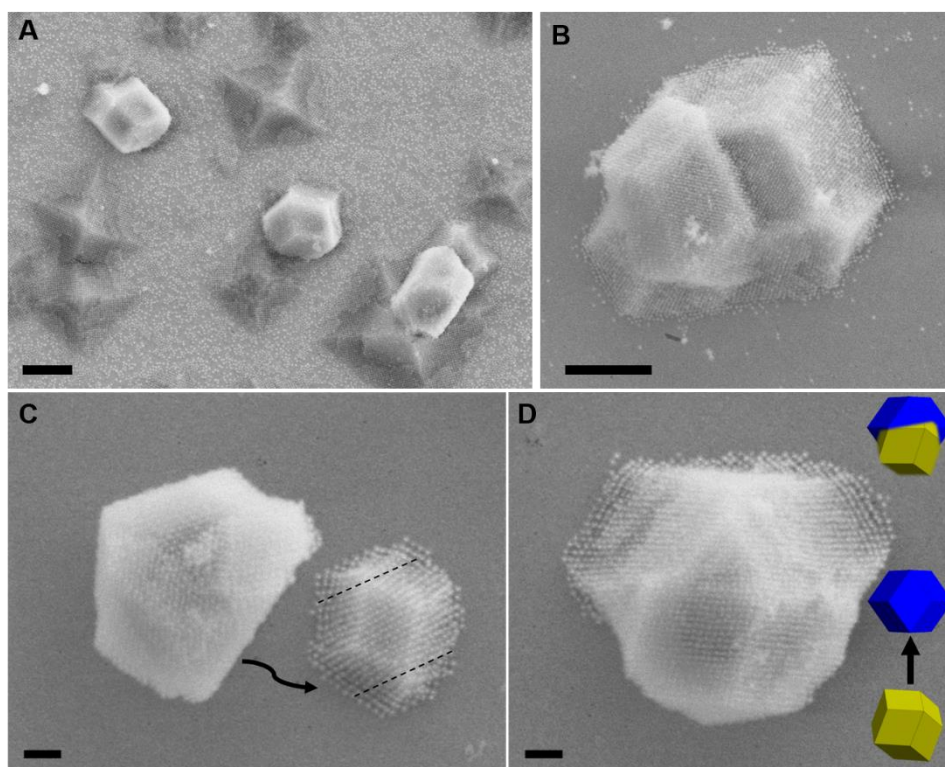
Some substrates used for PAE deposition contained microscopic scratches across their surface; this resulted in higher crystal densities at the scratches compared to the surrounding substrate. Additionally, sufficient nucleation density along a scratch resulted in elongated crystals aligned with the scratch direction (Supplementary Figure 19). It is hypothesized that the scratches occurred prior to gold coating and DNA functionalization of the slide, meaning that the higher exposed surface area at the scratch resulted in a higher DNA density that recruited and trapped nanoparticles diffusing across the surface, thereby promoting aligned crystal growth. Further evidence supporting this hypothesis comes from the fact that substrates functionalized with only 25% active linker loading exhibited the vast majority of their crystals directly on these scratches.



Supplementary Figure 19: Alignment to scratches. Both bi-functionalized (A) and mono-functionalized (B) substrates show preferential crystal alignment and growth along cracks. Additionally, on substrates functionalized with 25% active strands, the vast majority of crystals are grown from scratches (C), suggesting that the placement of crystals can be tailored by appropriate substrate patterning. Scale bars are 2 μ m.

6. *Surface-Induced Reorganization of Solution-Grown Wulff Polyhedra*

During the deposition and growth of Winterbottom constructions, particles in solution would often simultaneously nucleate and grow into Wulff polyhedra. Although the substrate was typically vertically oriented during crystal growth to prevent adhesion of these solution phase crystallites upon sedimentation, some crystals initially formed in solution did adhere to either the DNA-functionalized substrate or substrate-grown Winterbottom constructions and began to reform (Supplementary Figure 20). Most Wulff polyhedra that were observed to adhere to Winterbottom constructions formed grain boundaries between the two crystals that were not annealed out during the crystallization process. This does not preclude the process of Ostwald ripening or oriented reattachment processes that consumed the Wulff polyhedra and made their constituent PAEs part of the Winterbottom construction, but solution-grown crystallites that were either consumed by or



Supplementary Figure 20: During experiments, crystals from solution sometimes deposited and merged with substrate-bound crystals (A, B). When crystals deposit directly onto a substrate, they can reform through surface diffusion (C), where shape adopts pointy geometry. The crystal on the left in (C) was deposited from solution, and the crystal on the right is hypothesized to be the missing fragment of the crystal that rearranged to better adhere to the surface in the correct orientation; the dotted black lines show where Winterbottom shape would end. However when crystals exhibit bulk rearrangement, the crystal adopts the Winterbottom shape (D) (insets show how crystal has reformed). (C) and (D) occurred near each other on the same substrate, indicating that these processes can both occur under similar annealing conditions. Scale bars are 1 μ m in A,B, and 200 nm in C,D.

integrated into the Winterbottom construction would inherently be unobservable (i.e. they would result in single crystals that would be indistinguishable from larger than average Winterbottom constructions). Interestingly, however, when a crystal landed on bare (DNA-coated) substrate and underwent bulk rearrangement, it would typically take on the thermodynamically preferred Winterbottom shape (S20D). Conversely, when PAEs appeared to have detached from the original crystal and migrated on the surface to reform into another crystal (C), the shapes exhibited the “points” noted in the main text. This further supports the hypothesis that the points are a kinetic structure formed through substrate-bound nanoparticles migrating to the edge of the crystals.

Supplementary References

1. Macfarlane, R. J. *et al.* Nanoparticle Superlattice Engineering with DNA. *Science* **334**, 204–208 (2011).
2. Hurst, S. J., Lytton-Jean, A. K. R. & Mirkin, C. A. Maximizing DNA Loading on a Range of Gold Nanoparticle Sizes. *Anal. Chem.* **78**, 8313–8318 (2006).
3. Hill, H. D., Millstone, J. E., Banholzer, M. J. & Mirkin, C. A. The Role Radius of Curvature Plays in Thiolated Oligonucleotide Loading on Gold Nanoparticles. *ACS Nano* **3**, 418–424 (2009).
4. Bastús, N. G., Comenge, J. & Puntès, V. Kinetically Controlled Seeded Growth Synthesis of Citrate-Stabilized Gold Nanoparticles of up to 200 nm: Size Focusing versus Ostwald Ripening. *Langmuir* **27**, 11098–11105 (2011).
5. Hill, H. D. & Mirkin, C. A. The bio-barcode assay for the detection of protein and nucleic acid targets using DTT-induced ligand exchange. *Nat. Protoc.* **1**, 324–336 (2006).
6. Auyeung, E., Macfarlane, R. J., Choi, C. H. J., Cutler, J. I. & Mirkin, C. A. Transitioning DNA-Engineered Nanoparticle Superlattices from Solution to the Solid State. *Adv. Mater.* **24**, 5181–5186 (2012).
7. O'Brien, M. N., Radha, B., Brown, K. A., Jones, M. R. & Mirkin, C. A. Langmuir Analysis of Nanoparticle Polyvalency in DNA-Mediated Adsorption. *Angew. Chem. Int. Ed.* **53**, 9532–9538 (2014).
8. Senesi, A. J. *et al.* Stepwise Evolution of DNA-Programmable Nanoparticle Superlattices. *Angew. Chem. Int. Ed.* **52**, 6624–6628 (2013).
9. Thompson, C. V. On the grain size and coalescence stress resulting from nucleation and growth processes during formation of polycrystalline thin films. *J. Mater. Res.* **14**, 3164–3168 (1999).

10. Lewis, D. J., Gabrys, P. A. & Macfarlane, R. J. DNA-Directed Non-Langmuir Deposition of Programmable Atom Equivalents. *Langmuir* **34**, 14842–14850 (2018).
11. Auyeung, E. *et al.* DNA-mediated nanoparticle crystallization into Wulff polyhedra. *Nature* **505**, 73–77 (2014).
12. Zucker, R. V., Chatain, D., Dahmen, U., Hagège, S. & Carter, W. C. New software tools for the calculation and display of isolated and attached interfacial-energy minimizing particle shapes. *J. Mater. Sci.* **47**, 8290–8302 (2012).
13. Gabrys, P. A. & Macfarlane, R. J. Controlling Crystal Texture in Programmable Atom Equivalent Thin Films. *ACS Nano* (2019) doi:10.1021/acsnano.9b04333.
14. Lee, A. A., Perez-Martinez, C. S., Smith, A. M. & Perkin, S. Scaling Analysis of the Screening Length in Concentrated Electrolytes. *Phys. Rev. Lett.* **119**, 026002 (2017).
15. Zwanikken, J. W. & Cruz, M. O. de la. Tunable soft structure in charged fluids confined by dielectric interfaces. *Proc. Natl. Acad. Sci.* **110**, 5301–5308 (2013).
16. Li, Y., Girard, M., Shen, M., Millan, J. A. & Cruz, M. O. de la. Strong attractions and repulsions mediated by monovalent salts. *Proc. Natl. Acad. Sci.* **114**, 11838–11843 (2017).
17. Kewalramani, S. *et al.* Electrolyte-Mediated Assembly of Charged Nanoparticles. *ACS Cent. Sci.* **2**, 219–224 (2016).